Global and Planetary Change 162 (2018) 199–211

Contents lists available at ScienceDirect

Global and Planetary Change

journal homepage: www.elsevier.com/locate/gloplacha

Historical and future changes of frozen ground in the upper Yellow River Basin

Taihua Wang[a], Dawen Yang[a,*], Yue Qin[a], Yuhan Wang[a], Yun Chen[b], Bing Gao[c], Hanbo Yang[a]

[a] State Key Laboratory of Hydroscience and Engineering, Department of Hydraulic Engineering, Tsinghua University, Beijing 100084, China
[b] National Meteorological Center, China Meteorological Administration, Beijing 100081, China
[c] School of Water Resources and Environment, China University of Geosciences, Beijing 100083, China

ARTICLE INFO

Editor: Fabienne Marret-Davies

Keywords:
Seasonally frozen ground
Permafrost degradation
Upper Yellow River Basin
Stefan equation
Climate change

ABSTRACT

Frozen ground degradation resulting from climate warming on the Tibetan Plateau has aroused wide concern in recent years. In this study, the maximum thickness of seasonally frozen ground (MTSFG) is estimated by the Stefan equation, which is validated using long-term frozen depth observations. The permafrost distribution is estimated by the temperature at the top of permafrost (TTOP) model, which is validated using borehole observations. The two models are applied to the upper Yellow River Basin (UYRB) for analyzing the spatio-temporal changes in frozen ground. The simulated results show that the areal mean MTSFG in the UYRB decreased by 3.47 cm/10 a during 1965–2014, and that approximately 23% of the permafrost in the UYRB degraded to seasonally frozen ground during the past 50 years. Using the climate data simulated by 5 General Circulation Models (GCMs) under the Representative Concentration Pathway (RCP) 4.5, the areal mean MTSFG is projected to decrease by 1.69 to 3.07 cm/10 a during 2015–2050, and approximately 40% of the permafrost in 1991–2010 is projected to degrade into seasonally frozen ground in 2031–2050. This study provides a framework to estimate the long-term changes in frozen ground based on a combination of multi-source observations at the basin scale, and this framework can be applied to other areas of the Tibetan Plateau. The estimates of frozen ground changes could provide a scientific basis for water resource management and ecological protection under the projected future climate changes in headwater regions on the Tibetan Plateau.

1. Introduction

Frozen ground is an important component of the cryosphere and is vulnerable to climate warming; thus, it can serve as a sensitive indicator of climate change (Vaughan et al., 2013). Previous studies have reported that permafrost degradation is manifested by increases in the active layer thickness (ALT) and decreases in the areal extent (Frauenfeld, 2004; Li et al., 2008; Park et al., 2013; Wu et al., 2015; Luo et al., 2016), and this degradation profoundly impacts hydrological and ecological processes in high-latitude regions and alpine cold regions (Liu et al., 2011; Bense et al., 2012; Chen et al., 2012; Liu and Wang, 2012; Hayashi, 2013; Walvoord and Kurylyk, 2016; Y. Zhang et al., 2016). Similarly, the freeze-thaw cycle and thermal regimes of seasonally frozen ground are also undergoing considerable changes (Jin et al., 2015; K. Wang et al., 2015; Peng et al., 2016). Long-term changes in the maximum thickness of seasonally frozen ground (MTSFG) reflect changes in air temperature as well as the comprehensive effects of temperature seasonality, precipitation, land surface conditions and site-specific soil properties (Frauenfeld and Zhang, 2011; Peng et al., 2017). Although seasonally frozen ground is more widely distributed than permafrost (Zhang et al., 2003), long-term observations in regions with seasonally frozen ground remain limited, and the historical and potential future shifts in the soil thermal regime of seasonally frozen ground regions remain poorly understood.

The Tibetan Plateau (TP), also known as the third pole of the globe, has the largest area of alpine permafrost in the world (Qiu, 2008; Immerzeel et al., 2010; Cuo et al., 2015). Almost all of the TP is underlain by permafrost and seasonally frozen ground because of its high elevation (Guo and Wang, 2013). The source regions of several large Asian rivers, including the Yellow River, which is the second largest river in China (Hu et al., 2011), are located on the TP. Several studies have reported the degradation of frozen soil in the upper Yellow River Basin (UYRB), including an upward shift in the permafrost lower limit, shifts in the discontinuous/continuous permafrost boundary, and a decrease in the MTSFG at the point scale (Jin et al., 2009; Fang et al., 2011). These changes could generate complex interactions with wetland shrinkage, vegetation degradation and other ecohydrological changes resulting from climate change (Cheng and Wu, 2007; Jin et al.,

* Corresponding author.
E-mail address: yangdw@tsinghua.edu.cn (D. Yang).

https://doi.org/10.1016/j.gloplacha.2018.01.009
Received 7 October 2017; Received in revised form 1 January 2018; Accepted 8 January 2018
0921-8181/ © 2018 Elsevier B.V. All rights reserved.

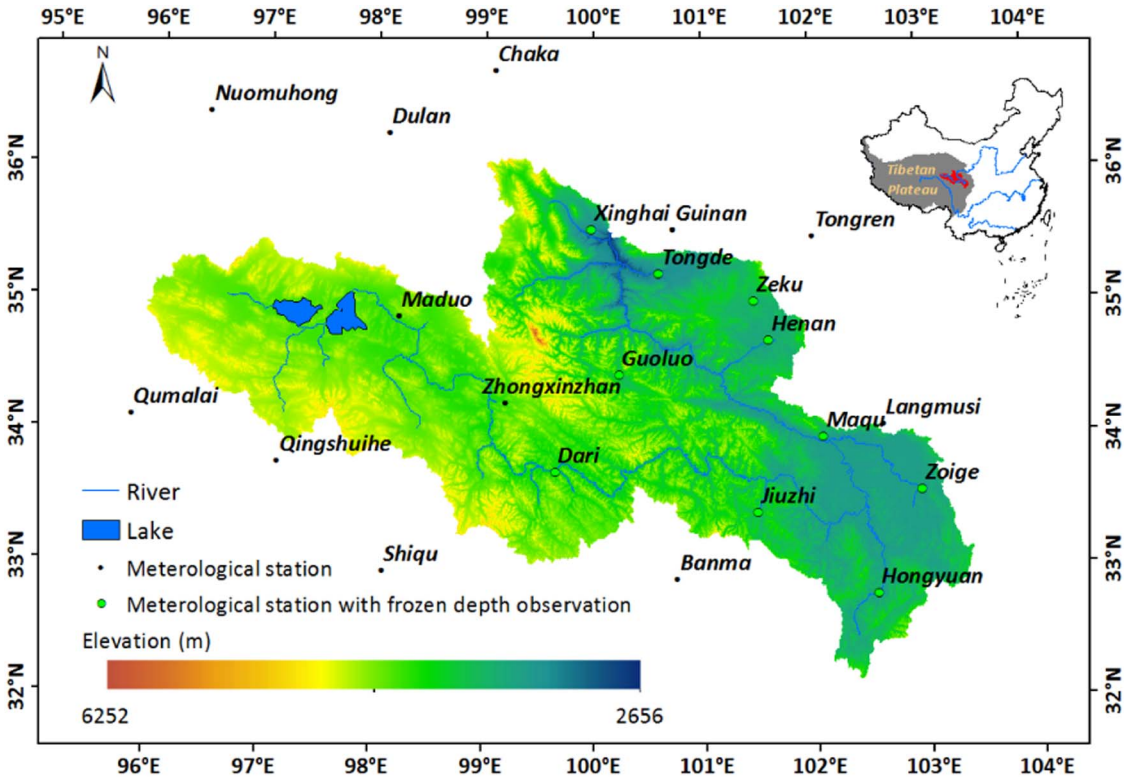

Fig. 1. Study area and locations of the meteorological stations. Ten stations have frozen depth records.

2009; Yang et al., 2010; Cuo et al., 2013; W.J. Zhang et al., 2016). Most of the previous studies focusing on changes in the frozen ground on the TP are based on point-scale borehole observations (Wu and Zhang, 2010; Xie et al., 2012; Wu et al., 2015), and few studies have focused on changes in frozen ground at the regional or catchment scale (Pang et al., 2011; Qin et al., 2016; Xu et al., 2016). Although several studies have predicted future changes in the frozen ground of the TP, they have only focused on changes in the permafrost (Nan et al., 2005; Pang et al., 2011; Guo et al., 2012), and none have projected long-term changes in regions with seasonally frozen ground.

Traditional frozen ground studies have only relied on in situ observations; however, due to the harsh climate in frozen ground regions, in situ observations are hard to obtain, very expensive, and usually restricted to the point scale (Zhang et al., 2005; Frauenfeld and Zhang, 2011; Wu et al., 2015). Therefore, freeze-thaw models can complement in situ observations, and this combination can be used to obtain long-term and spatially continuous frozen ground information at a larger scale if proper input data and parameterization methods are used (Riseborough et al., 2008; Walvoord and Kurylyk, 2016). The commonly used soil freeze-thaw models can be categorized into 2 groups: (1) analytical solution models and (2) numerical method models (Walvoord and Kurylyk, 2016). Numerical models that incorporate numerical solution schemes, such as finite element and finite difference methods, are usually more accurate in simulating ground freeze-thaw cycles if they are properly parameterized (Y.S. Zhang et al., 2008; Li et al., 2010). Nevertheless, accurate results are only obtained when a greater number of parameters are included, which requires more data input and leads to greater computational complexity (Walvoord and Kurylyk, 2016). Analytical algorithms based on certain assumptions can achieve considerable computational savings for simulations at large scales and introduce fewer parameters than numerical methods, and these algorithms include the Stefan equation, the Kudryavtsev model, and the temperature at the top of permafrost (TTOP) model (Riseborough et al., 2008; Yin et al., 2016). Due to limited data, many studies used a simplified Stefan equation that only considered the air temperature variability (Zhang et al., 2005; Q.F. Wang et al., 2015; Wu et al., 2015; Peng et al., 2017). The Stefan equation and TTOP model with physically based parameters combining multi-source data based on either ground or remote sensing observations could have the potential to better reflect the spatial variability of frozen ground.

In the headwater regions of major Asian rivers, such as the Yellow River, few studies have focused on the historical and future trends of frozen ground changes. Recently, Qin et al. (2017) used a process-based model GBEHM to simulate the frozen ground change in the UYRB, and they focused on the impacts of climate warming and consequent frozen ground changes on ecohydrology during 1981–2015. Our study uses two analytical algorithms, the Stefan equation and TTOP model, which call for fewer parameters and less computational complexity, and focuses on the long-term frozen ground changes in the UYRB both in the past (1965–2014) and in the future (2015–2050). The objectives of this study are to (1) test and verify the applicability of the Stefan equation and the TTOP model with physically based parameters, which may also be useful in the headwater regions of other major rivers originating from the TP; (2) understand the long-term changes and spatial variability in frozen ground over the past 50 years in the UYRB; and (3) project the response of frozen ground to future climate change in the UYRB.

2. Study area and data

2.1. Study area

The UYRB is located in the transitional zone between seasonally frozen ground and discontinuous and continuous permafrost on the northeastern TP (Jin et al., 2009). In this study, the UYRB refers to the catchment upstream of the Tangnaihai hydrological station, and it covers an area of 122,000 km^2 that accounts for 16% of the total area of the Yellow River Basin and yields 35% of the total runoff of the Yellow River (Hu et al., 2011). The elevation of the UYRB ranges from 2656 m to 6350 m (Fig. 1) and mainly decreases from southwest to northeast. A

long-term mean annual air temperature of −2.1 °C and a long-term mean annual precipitation of 541.5 mm are observed in the region (Hu et al., 2011). Investigations in 1978 indicated that the UYRB had > 5000 lakes (Xu, 2015), with the largest being Eling Lake and Zaling Lake. The Zoige wetland is located in the southeastern UYRB, and it is one of the largest alpine wetlands on the TP and is dominated by helophyte species (W.J. Zhang et al., 2016). Several studies in recent years have reported that climate change in the UYRB has caused the degradation of frozen soil, the lowering of the groundwater level, the shrinkage of lakes and wetlands, the degradation of vegetation and the desertification of the landscape (Jin et al., 2009; Yang et al., 2010; W.J. Zhang et al., 2016).

2.2. Data

The daily mean air temperature data during 1965–2015 of the 22 meteorological stations (Fig. 1) located within and around the UYRB are from the National Meteorological Information Center (NMIC) of the China Meteorological Administration (CMA) (http://data.cma.cn). Gridded air temperature data with 1-km resolution are interpolated from gauge observations using an angular distance weighting method (Yang et al., 2004) and adjusted by elevation. The gridded precipitation data are spatially interpolated from the site observations using a method called China Gauge-based Daily Precipitation Analysis (CGDPA) proposed by Shen and Xiong (2016). Digital elevation data with a resolution of 90 m are from the Shuttle Radar Topography Mission (SRTM) (Jarvis et al., 2008). The soil property data used in this study, including the soil type, texture and bulk density, are from the Harmonized World Soil Database (HWSD) (FAO and ISRIC, 2009) and were downloaded from the website of the Cold and Arid Regions Science Data Center at Lanzhou (CARD) (http://westdc.westgis.ac.cn).

The ground surface temperature data and the frozen soil depth observations at 10 stations (marked in Fig. 1) located in the UYRB are also from the CMA. In accordance with the CMA (2007b), the daily frozen depth is manually measured by the standard frozen soil apparatus. The apparatus is vertically buried in the meteorological field, and the frozen depth is measured by the length of ice in the inner rubber tube. The temporal ranges of available data vary among different stations (see Table 1), and most stations have continuous frozen soil depth data during 1967–2014. In accordance with the CMA (2007a), ground surface temperatures were measured with a mercury ball thermometer (ball diameter of approximately 3 mm). Although measurement standards state that half of the thermometer sensor should be buried in the ground and the other half exposed to the air, in practice, the sensors were usually buried more than halfway and were often colored white to reduce solar heating (K. Wang et al., 2015). The ground surface temperatures are available during 1967–2014 for all the stations except the Tongde and Zeku stations. This study also collected data at 30 boreholes in the UYRB drilled in 2010 and 1988. Frozen ground type and permafrost thickness data were obtained from all 30 boreholes, and the mean annual ground temperature (MAGT) at zero annual amplitude depth was obtained from the 10 boreholes drilled in 2010 (Jin et al., 2009).

In addition to the ground-based observations, remote sensing-based data are also used to determine the spatial variability of certain variables that can influence frozen ground. The MODIS Land Surface Temperature (LST) data used in this study were the 1-km gridded clear-sky MOD11A2 (Terra MODIS) and MYD11A2 (Aqua MODIS) products (reprocessing version 5) during 2003–2012 (Wan, 2007). Both MOD11A2 and MYD11A2 provide two observations (daytime and nighttime), which means that there are four LST observations for the same pixel per day. This study adopts the 0–100 cm depth soil moisture data from the China Soil Moisture Dataset from Microwave Data Assimilation (CSMDA) (http://en.tpedatabase.cn) (Yang et al., 2016). This dataset assimilates passive microwave data (AMSR-E TB) through a Dual-Pass Microwave Land Data Assimilation System and was validated to have ± 5% volumetric water content accuracy for the TP (Yang et al., 2016).

The projected daily mean air temperature and daily precipitation from 5 GCMs, i.e., NorESM1-M, MIROC-ESM-CHEM, IPSL-CM5A-LR, HadGEM2-ES and GFDL-ESM2M, are used to project future frozen ground changes. The data are provided by the Inter-Sectoral Impact Model Intercomparison Project (ISI-MIP) (Warszawski et al., 2014) and have been corrected by a statistical bias correction method (Piani et al., 2010) using the gauge data across China and transformed to ASCII code by the Institute of Environment and Sustainable Development in Agriculture, Chinese Academy of Agricultural Sciences. These data include historical data from 1961 to 2000 and projected data from 2001 to 2050 under different Representative Concentration Pathways (RCPs), and they were also adopted by another study (Chen et al., 2017). In this study, the air temperature and precipitation data from the 5 GCMs under the RCP 4.5 scenario with 0.5° spatial resolution are used. We did not downscale the monthly precipitation data, but downscaled the air temperature data to a 1-km resolution by using the rate of change in air temperature with increasing elevation obtained from the historical observations. All 5 GCMs project a warm-moist change mode in the future, although the GCMs present different rates of change and different spatial patterns.

Table 1
Comparison of observed and Stefan equation-estimated maximum thickness of seasonally frozen ground (MTSFG) at 10 meteorological stations.

Station name	Elevation (m a.s.l.)	c_f	n_f	Observed multi-year average MTSFG (cm)	Estimated multi-year average MTSFG (cm)	Correlation coefficient r	p-Value	*RMSE* (cm)	Observed long-term MTSFG trend (cm/10 a)	Estimated long-term MTSFG trend (cm/10 a)	Observation period
Tongde	3080.0	0.16	0.56	124.60	115.70	0.494	.000	14.78	−4.12*	−4.75*	1967–2014
Xinghai	3323.2	0.12	0.67	158.57	155.91	0.787	.000	13.77	−8.43*	−6.61*	1967–2014
Zoige	3441.4	0.16	0.51	60.96	85.99	0.359	.016	26.29	−0.08	−3.23*	1970–2014
Maqu	3471.4	0.24	0.46	79.00	85.96	0.662	.000	11.57	−7.19*	−4.18*	1980–1996, 2006–2014
Hongyuan	3491.6	0.20	0.51	50.90	81.99	0.608	.000	32.27	−2.87	−2.67*	1970–1978, 1994–2014
Henan	3500.0	0.12	0.75	122.23	136.13	0.865	.000	16.37	−10.75*	−6.86*	1980–2014
Jiuzhi	3628.5	0.24	0.44	92.52	100.25	0.641	.000	15.88	−10.61*	−2.35*	1973–2014
Zeku	3662.8	0.08	0.78	183.65	186.25	0.697	.000	15.76	−11.38*	−5.39*	1967–2014
Guoluo	3719.0	0.20	0.58	164.16	143.94	0.740	.000	24.78	−9.53*	−5.23*	1967–2014
Dari	3967.5	0.20	0.67	195.63	168.56	0.627	.000	29.58	−3.61	−5.57*	1967–2014

*Note: c_f relates to the soil water retention capacity, as mentioned in Eq. (2) and calibrated by the CSMDA dataset, and n_f is the freezing season n-factor calculated from MODIS LST. The correlation coefficient r, p-value, and root mean square error (*RMSE*) between the observed and estimated MTSFG values are also shown for evaluation. An asterisk following a value means the trend is significant at the 0.05 significance level.

3. Methods

3.1. Simulating the maximum thickness of seasonally frozen ground

The basic form of the Stefan equation can be expressed as follows (Woo, 2012; Q.F. Wang et al., 2015):

$$MTSFG = \sqrt{2\lambda_f n_f \tau / L\rho_l \theta_f}\ \sqrt{DDF_a}, \quad (1)$$

where *MTSFG* is the maximum depth from the ground surface to the freezing front in a freezing season (m); λ_f is the thermal conductivity of frozen soil (W/(m °C)); n_f is the freezing n-factor; τ is the unit conversion coefficient (8.64×10^4 s/day); L is the latent heat of fusion (3.34×10^5 J/kg); ρ_l is the density of liquid water (1.00×10^3 kg/m^3); θ_f is the volumetric liquid water content before soil freezing (m^3/m^3); DDF_a is the air freezing index over a freezing year (°C day), and a freezing year is defined as the period between July of one year and June of the following year.

For each grid, DDF_a is calculated by summing up all the daily mean air temperature lower than 0 °C in a freezing year (Frauenfeld et al., 2007). θ_f is determined by a variant of the antecedent precipitation index method (Teng et al., 1993; Lee and Huang, 2013), expressed as:

$$\theta_f = a_f P_{Sep} + a_f b_f P_{Aug} + a_f b_f^2 P_{Jul} + c_f, \quad (2)$$

where P_{Sep}, P_{Aug} and P_{Jul} are the precipitation amounts in September, August and July (mm); a_f and b_f are parameters related to the soil water retention capacity and the attenuation rate of antecedent precipitation, and c_f represents the soil moisture before freezing after a long-duration drought. The values of a_f, b_f and c_f for each grid are calibrated by the average 0–100 cm September soil water content during 2002–2010 from CSMDA dataset. Notably, the September soil water content can represent the soil moisture before freezing, since there are few differences among the soil water contents in September, October and November. The volumetric liquid water content is set to have a lower limit of 0.12 and cannot exceed the saturated soil moisture content.

Using Eq. (2), the interannual variability in soil water content resulting from precipitation fluctuations can be reflected. The thermal conductivity of frozen soil (λ_f) is determined by Johansen's parameterization scheme (Farouki, 1981) using θ_f and the soil properties provided by FAO and ISRIC (2009). More details about Johansen's scheme can be found in Qin et al. (2016). The parameterization of n_f will be introduced in Section 3.3.

3.2. Estimating permafrost distribution

In this research, the TTOP model is adopted to estimate the permafrost distribution. The TTOP model can be expressed as follows (Riseborough et al., 2008; Zhao et al., 2017; Zou et al., 2017):

$$TTOP = (\lambda_t n_t DDT_a/\lambda_f - n_f DDF_a)/P, \quad (3)$$

where λ_t is the thermal conductivity of thawed soil (W m^{-1} °C^{-1}); n_t is the thawing n-factor; DDT_a is the air thawing index (°C day); and P is the annual period (365 days). This study uses the negative or positive value of TTOP for judging whether permafrost exists. From Eq. (3), if $n_f DDF_a$ is greater than $\lambda_t n_t DDT_a/\lambda_f$, then TTOP will be below 0 °C and permafrost exists. Under this circumstance, TTOP represents the mean annual temperature at the top of permafrost (°C), which can reflect permafrost stability; otherwise, there is only seasonally frozen ground. The TTOP model is an equilibrium model (Riseborough, 2007; Ran and Li, 2016); to alleviate the transient effects, this study chooses the mean TTOP of a relatively long period, 20 years, to estimate the permafrost distribution.

The determination of the parameters in the freezing season has already been introduced in Section 3.1. Similarly, for each grid, DDT_a is calculated by summing up all the daily mean air temperatures higher than 0 °C in a normal year (Frauenfeld et al., 2007). θ_t, representing soil water content in the thawing season, is considered as the function of the precipitation in the thawing season (Pan et al., 2003), and in this study it is calculated as follows:

$$\theta_t = a_t (P_{Jul} + P_{Aug} + P_{Sep}) + c_t, \quad (4)$$

where a_t and c_t are parameters related to the soil properties and are calibrated by the average 0–100 cm July–September soil water content during 2002–2010 from the CSMDA dataset. The thermal conductivity of thawed soil (λ_t) is also determined by Johansen's parameterization scheme (Farouki, 1981; Qin et al., 2016) using θ_t and the soil properties provided by FAO and ISRIC (2009). The parameterization of n_t will be introduced in Section 3.3.

3.3. Parameterization method of the n-factor

The freezing n-factor (n_f) and thawing n-factor (n_t) in Eqs. (1) and (3) represent the energy balance between the ground surface and the near-surface atmosphere, and the equations are as follows (Klene et al., 2001):

$$n_f = DDF_g/DDF_a, \quad (5a)$$

$$n_t = DDT_g/DDT_a, \quad (5b)$$

where DDF_g and DDT_g are ground surface freezing index and thawing index, respectively, calculated by summing the daily ground surface temperatures lower than and higher than 0 °C, respectively, in a freezing year or a normal year. Ground surface temperature (GST) observations are available at meteorological stations; however, they can only obtain n-factor data at the point scale, while MODIS LST data can provide spatial distribution information. In this study, a multiple linear regression was employed to distribute different weights to each MODIS LST observation to establish a daily mean GST empirical model, and the processing details are described in Zou et al. (2014). The parameters in the empirical model were calibrated using the GST observations at the meteorological stations in URYB during 2003–2012. In this study, the empirical formula is as follows:

$$GST = 0.170 \times Terra_{day} + 0.307 \times Terra_{night} + 0.111 \times Aqua_{day} + 0.442 \times Aqua_{night} + 5.564, \quad (6)$$

where *GST* is the daily mean ground surface temperature; $Terra_{day}$, $Terra_{night}$, $Aqua_{day}$, and $Aqua_{night}$ are respectively the MOD11A2 (Terra MODIS) and MYD11A2 (Aqua MODIS) daytime/nighttime LST products. The correlation coefficient, mean error and root mean squared error between the observed GST and the GST estimated by Eq. (6) were respectively 0.95 to 0.98, −0.45 to 0.47 °C, and 2.01 to 2.49 °C at the stations. Therefore, the spatial distribution of daily GST can be calculated from MODIS LST data using Eq. (6), which is thereafter used to calculate the spatial distribution of DDF_g. The spatial distribution of n_f and n_t were calculated using the spatial distribution of DDF_g derived from MODIS LST and the DDF_a derived from the interpolated daily air temperature, and the mean values of n_f and n_t during 2003–2014 were used as the long-term n_f and n_t values (Fig. 2).

3.4. Trend detection and simulation performance evaluation

The temporal trends in this study are calculated by the slope of the line fitted by the least square method. The Mann-Kendall nonparametric test is applied in this study to detect the significance of trends in long-term time series (Yang et al., 2004), and a significance level of 0.05 is chosen for all trend analyses in this study.

Pearson's correlation coefficient (r) and root mean squared error (*RMSE*) are selected as the evaluation indicators. The p-value of correlation was also calculated, and a p-value lower than .05 indicates the correlation is significant at the 0.05 significance level (Krause et al., 2005).

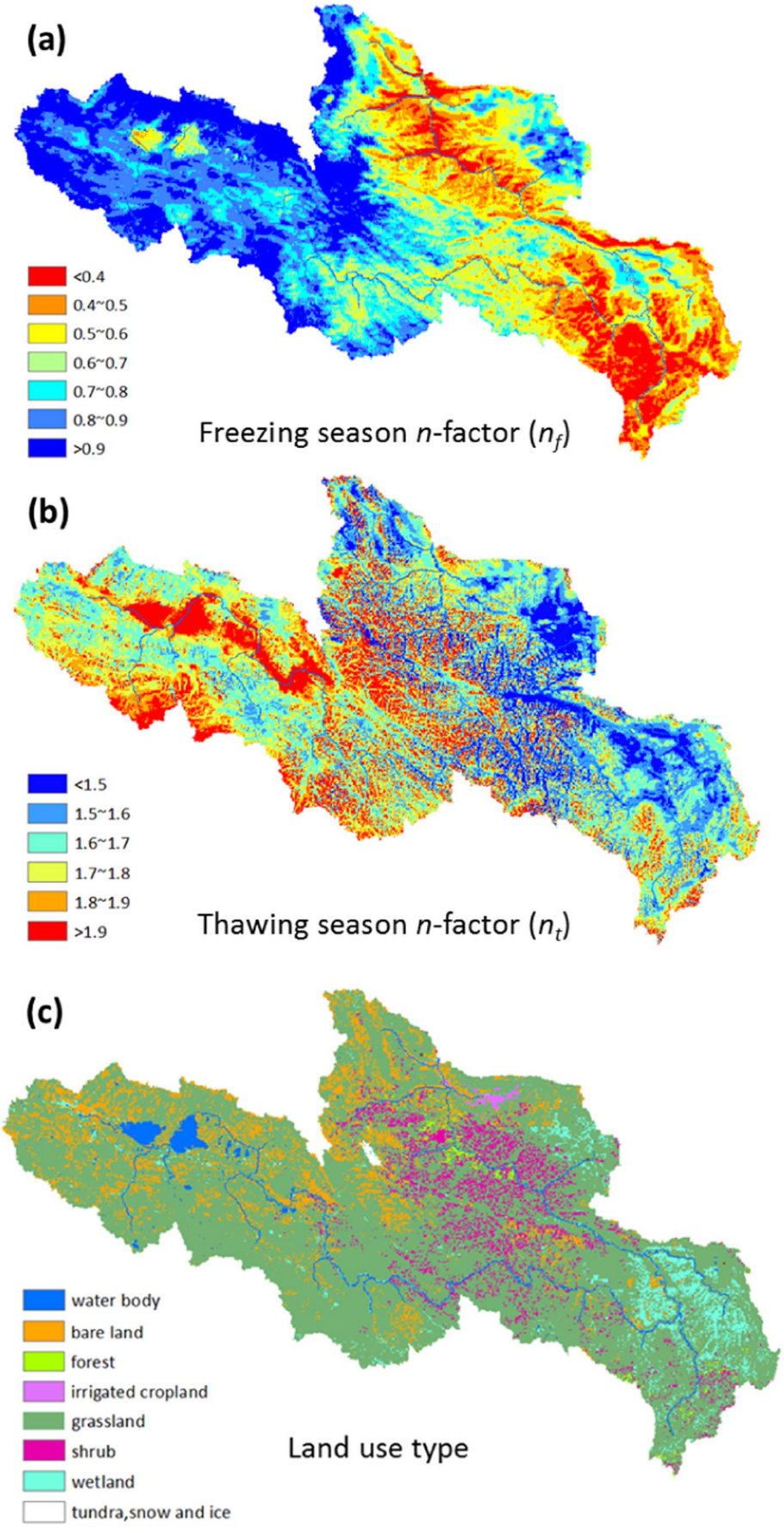

Fig. 2. Spatial distribution of (a) the freezing season n-factor (n_f), (b) the thawing season n-factor (n_t) derived from MODIS LST and (c) the land use map.

4. Results

4.1. Historical change in the maximum thickness of seasonally frozen ground

The soil frozen depths at the 10 stations in the UYRB (marked in Fig. 1) were observed, and the data are mainly available during the period 1967–2014. Table 1 shows the observed multi-year average MTSFG values and trends at 10 stations in order of increasing elevation. The deepest multi-year average MTSFG occurred at Dari station (195.63 cm), which features the highest elevation (3967.5 m a.s.l.) among the 10 stations. The shallowest multi-year average MTSFG occurred at Hongyuan station (50.90 cm) located within the Zoige wetland. Although the elevation at Hongyuan station is not the lowest, its relatively high soil water retention capacity ($c_f = 0.20$, introduced in Eq. (2)) and relatively low freezing season n-factor ($n_f = 0.51$) collectively result in a shallow frozen depth. The MTSFG decreased by 11.38 cm/10 a during 1967–2014 at Zeku station, which was the most rapid among the 10 stations, whereas the MTSFG decreased insignificantly at Zoige station and Hongyuan station. The rates of MTSFG decrease tend to be larger at stations with higher elevations during the past 50 years in the UYRB (Table 1).

The MTSFG observations at the 10 stations are used to validate the estimated results derived from the Stefan equation. The estimated MTSFG values are compared with all available observed MTSFG values from the 10 meteorological stations over the past 50 years (Fig. 3). Although the simulated results tend to overestimate the MTSFG at the stations with a shallow frozen depth and underestimate the MTSFG at the stations with a deep frozen depth, they show a significant linear relationship with the observed values, with an r value of 0.935 and *RMSE* of 21.25 cm. The estimated MTSFG values have a satisfactory linear relationship with the observed MTSFG values ($p < .05$) at all the 10 stations (Table 1). Eight of the 10 stations had r values larger than 0.6, and 6 of the 10 stations had *RMSE* values < 20 cm, thereby verifying the applicability of the Stefan equation to the simulation of MTSFG values. The estimated results tend to underestimate the MTSFG decreasing rate at most stations, especially at Henan, Zeku and Jiuzhi stations. However, the biases in the long-term MTSFG decreasing trend at the other stations are < 3.5 cm/10 a.

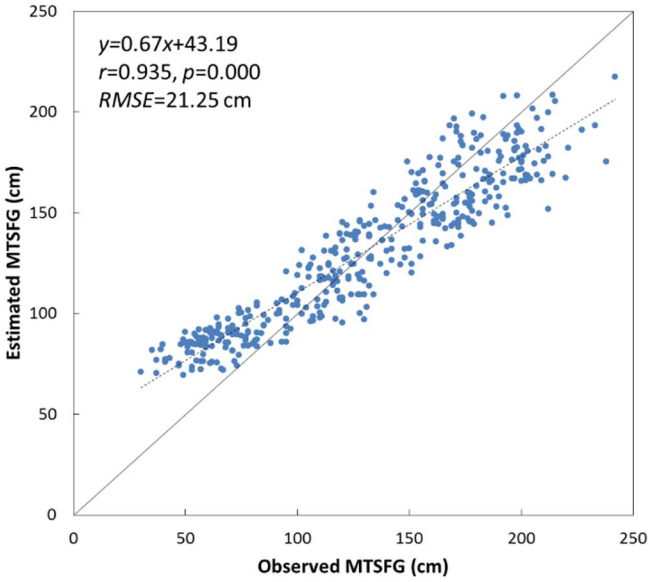

Fig. 3. Comparison of the MTSFG estimated by the Stefan equation with the observed MTSFG at 10 meteorological stations from 1967 to 2014.
Note: The equation of linear regression, the values of the correlation coefficient (r), the p-value and root mean squared error (*RMSE*) are labeled. The linear regression line is shown as a dashed line.

Fig. 4 illustrates the interannual variations in the areal mean MTSFG estimated by the Stefan equation and the mean annual air temperature (MAAT) for each freezing year starting in July over the seasonally frozen ground region. The areal mean MAAT in seasonally frozen ground region increased from −1.75 to 0.41 °C, which represented an increasing rate of 0.42 °C/10 a during 1965–2014. Consequently, the areal mean MTSFG decreased from 133.13 cm in 1965 to 107.91 cm in 2014, which represented a decreasing rate of 3.47 cm/10 a, and the net decrease was 25.2 cm over the past 50 years. The interannual variations in MTSFG and MAAT show similar fluctuation patterns but are not exactly the same, and the acceleration in the rate of MTSFG decrease is consistent with the acceleration in the rate of MAAT increase since 1995.

The spatial distribution of the 50-year mean MTSFG estimated by the Stefan equation during 1965–2014 is shown in Fig. 5a. The extent of the seasonally frozen ground region is determined by the TTOP model. Although the elevation of the southeastern Zoige wetland is not the lowest in the UYRB, this area has the shallowest MTSFG < 100 cm because of its high water content and the relatively large difference between the air and ground temperatures, which is related to the typical nature of wetlands. The rate of change in MTSFG during 1965–2014 varied from −7.6 to 1.3 cm/10 a estimated by the Stefan equation, with an areal mean value of 3.47 cm/10 a (Fig. 5b). Almost all grids show a significant decreasing MTSFG trend. The most dramatic MTSFG decrease occurs at the transitional zone between permafrost and seasonally frozen ground around Xinghai station (Fig. 5b).

4.2. Historical change in the permafrost distribution

In this study, the TTOP model is adopted to estimate the permafrost distribution changes in the UYRB. Point-scale observations from boreholes drilled in 2010 and 1988 are compared with the results derived from the TTOP model for validation (Table 2, Figs. 6 and 7). The values of the observed mean annual ground temperature (MAGT) at the zero annual amplitude depth at the 10 boreholes drilled in 2010 are close to the mean TTOP during 2005–2014 (Fig. 6b). The permafrost thicknesses at the 20 boreholes drilled in 1988 and the 10 boreholes drilled in 2010 are plotted against the corresponding TTOP values calculated by the TTOP model (Fig. 8a), and the geothermal gradient values at most boreholes range from 2.5 to 10 °C/100 m, which are close to the estimate from previous investigations on the TP (Wu et al., 2010). The frozen ground types of most of the boreholes are correctly estimated by the TTOP model (Table 2 and Fig. 6a), except YNG-2 in 2010 and 5 boreholes in 1988. The incorrect estimates of the frozen ground type might be attributed to scale inconsistency. Therefore, the TTOP model is applicable in estimating the permafrost distribution in the UYRB.

As estimated from the TTOP method, permafrost occurred in 48.6% of the UYRB area (60,125 km^2) in Period 1 (1971–1990), whereas permafrost occupied only 37.5% of the UYRB area (46,394 km^2) in Period 2 (1991–2010). According to the results derived from the TTOP model, approximately 22.8% of the permafrost in the UYRB degraded into seasonally frozen ground over the past 50 years. In Fig. 7, the pink area shows where the degradation from permafrost into seasonally frozen ground occurred. Previous investigations have shown that Maduo Town was underlain by permafrost in the 1970s but was no longer underlain by permafrost after the 1990s (Jin et al., 2009; Luo et al., 2012b), which is consistent with the permafrost distribution change estimated by the TTOP model (Fig. 7). Moreover, investigations have also found that permafrost was present at boreholes XXH-1 and YNG-3 in the 1990s but totally absent by 2010 (Luo et al., 2012a). These observational results are also consistent with the estimates derived from the TTOP model (Fig. 7).

4.3. Change in frozen ground under future climate scenarios

Using the daily air temperature and precipitation data projected by

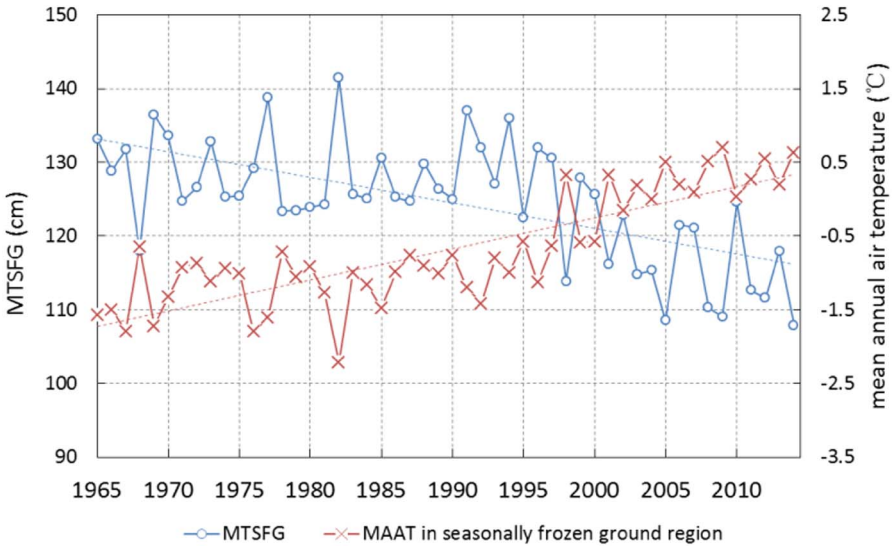

Fig. 4. Interannual variations in the areal mean MTSFG estimated by the Stefan equation and the mean annual air temperature (MAAT) over the past 50 years.

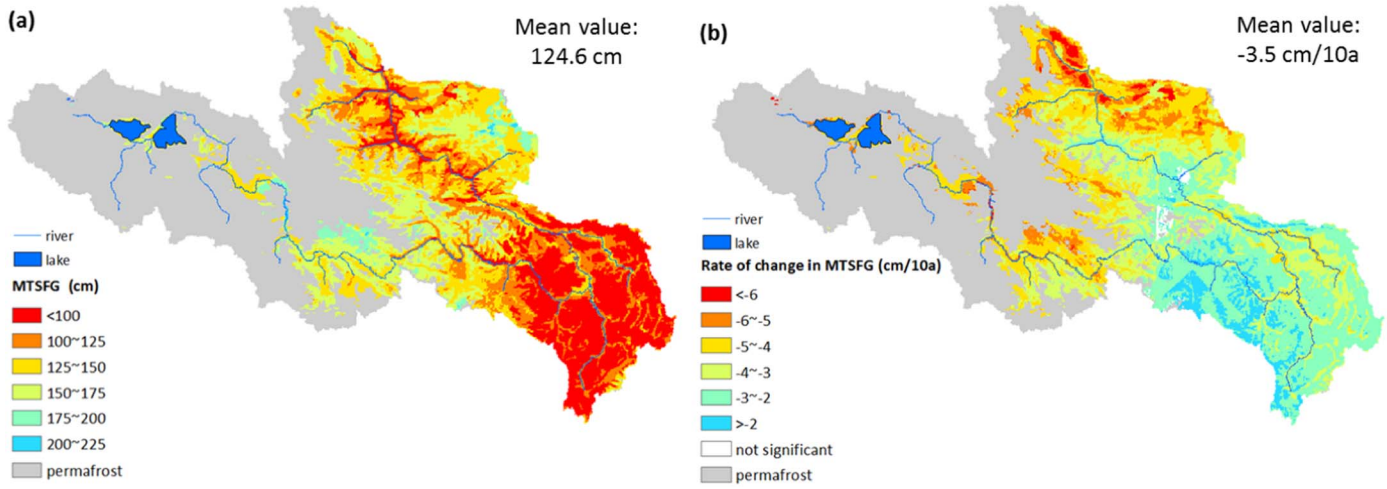

Fig. 5. Spatial distribution of (a) the 50-year mean MTSFG (cm) and (b) the rate of change in MTSFG (cm/10 a) estimated by the Stefan equation during 1965–2014 with a significance level of 0.05.

5 different climate models under the RCP 4.5 scenario, possible future frozen ground changes, including changes in the MTSFG and the permafrost distribution, are estimated. We adopt the fixed seasonally frozen ground extent using the mean TTOP in 1965–2014 to obtain areal mean values. The MAAT values in the historical period (1965–2014) are overestimated for all 5 GCMs compared with the observed MAAT values, resulting in an underestimation of the historical MTSFG estimated by the Stefan equation using GCM historical data compared with that using historical observed data (Table 3). The historical long-term MTSFG trend derived from IPSL-CM5A-LR (−3.08 cm/10 a) is closest to the trend derived from the historical observed data (−3.47 cm/10 a). In the future period (2015–2050), the five GCMs under the RCP 4.5 scenario project different MTSFG decreasing rates (Fig. 8 and Table 3), with the most rapid decreasing rate of 3.07 cm/10 a projected by the MIROC-ESM-CHEM model and the slowest decreasing rate of 1.69 cm/10 a projected by the GFDL-ESM2M model. The mean of the 5 GCMs projects a MTSFG decreasing rate of 2.47 cm/10 a during 2015–2050.

Using the TTOP model, historical and future permafrost distributions are estimated by the 5 GCMs under the RCP 4.5 scenario (Table 4). The mean of the 5 GCMs projects a decline in the permafrost area from 44,235 km^2 during 1991–2010 to 26,935 km^2 during 2031–2050. The largest estimate for permafrost area during 2031–2050 is 33,867 km^2 in the GFDL-ESM2M model (a 26.5% decrease compared with 1991–2010), and the smallest estimate for permafrost area during 2031–2050 is 18,633 km^2 in the MIROC-ESM-CHEM model (a 57.9% decrease compared with 1991–2010) (Table 4). These estimates predict that approximately 40% of the current permafrost in the UYRB will degrade to seasonally frozen ground in the first half of the 21st century.

5. Discussion

5.1. Stefan equation with physically based parameters: applicability and limitations

The Stefan equation is derived using several assumptions, including uniform thermal conductivity, heat gain or loss via conduction and negligible sensible heat (Woo, 2012; Walvoord and Kurylyk, 2016). In the UYRB, the soil moisture content is relatively high, and the assumption of negligible sensible heat can be met (Kurylyk and Hayashi, 2016). Our findings indicate that feasible and reliable estimates of long-term change and spatial variability at the basin scale can be derived using the Stefan equation in the UYRB, and it could also be used in other source areas of major rivers in cold regions.

The complete form of the Stefan equation is shown in Eq. (1), but many previous studies (Zhang et al., 2005; Q.F. Wang et al., 2015; Wu

Table 2
Borehole information and validation of the frozen ground type estimated by the TTOP model.

Borehole	Latitude	Longitude	Elevation (m a.s.l.)	Drilling time	Permafrost thickness (m)	MAGT (°C)	Observed type	Estimated type
CLP-1	34°15′	97°51′	4727	2010/8	78	−1.81	PF	PF
CLP-2	34°15′	97°51′	4723	2010/8–9	74	−1.72	PF	PF
CLP-3	34°16′	97°52′	4663	2010/8	53	−1.25	PF	PF
CLP-4	34°19′	97°54′	4564	2010/8	35	−0.70	PF	PF
YNG-1	34°24′	97°57′	4452	2010/8	17	−0.22	PF	PF
YNG-2	34°26′	97°56′	4395	2010/8	/	1.34	SFG	PF
YNG-3	34°30′	97°58′	4333	2010/8	/	1.01	SFG	SFG
XXH-1	34°39′	98°26′	4231	2010/8	/	0.52	SFG	SFG
MDB	34°51′	98°33′	4225	2010/9	37	−0.73	PF	PF
K445	34°58′	98°33′	4288	2010/9	45	−0.96	PF	PF
ZK5	34°53′	98°11′	4220	1988	10	/	PF	PF
ZK6	35°05′	97°46′	4272	1988	6.5/4.45	/	PF	PF
ZK7	35°12′	97°43′	4472	1988	44.27	/	PF	PF
ZK8803	35°10′	97°42′	4400	1988	18.2	/	PF	PF
ZK8804	35°01′	97°42′	4275	1988	8.25	/	PF	SFG
ZK8805	35°08′	97°45′	4300	1988	6.5	/	PF	PF
No5	35°04′	98°05′	4239	1988	26.5	/	PF	PF
No7	34°56′	98°13′	4280	1988	/	/	SFG	PF
No8	34°55′	98°31′	4253	1988	19.2	/	PF	PF
No9	34°50′	98°08′	4216	1988	5.1	/	PF	SFG
No10	34°49′	98°22′	4218	1988	17.8	/	PF	PF
K1	34°54′	96°20′	4583	1988	1.7	/	PF	PF
K2	34°53′	96°20′	4507	1988	3.3/15.0	/	PF	PF
K3	34°59′	97°48′	4272	1988	/	/	SFG	SFG
K4	34°44′	96°09′	4557	1988	26	/	PF	PF
K5	34°43′	96°09′	4569	1988	19.8	/	PF	PF
K8	34°52′	98°10′	4211	1988	/	/	SFG	PF
K14	34°54′	98°11′	4221	1988	8.5	/	PF	PF
K10	34°01′	98°08′	4294	1988	2.35	/	PF	PF
ZK4	34°00′	98°03′	4220	1988	/	/	SFG	PF

Note: PF = PF, SFG = SFG, "/" means not applicable, MAGT = mean annual ground temperature at the zero annual amplitude depth.

et al., 2015; Peng et al., 2017) have used the following simplified Stefan equation to estimate the MTSFG or ALT values:

$$MTSFG = E\sqrt{DDF_a}. \quad (7)$$

This simplified equation only considers fluctuations in the air freezing or thawing index and regards the remaining parameters as the time-invariant edaphic parameter E; thus, it neglects the interannual variability in soil properties. In addition, previous studies obtained the spatial distribution of E by interpolation from station-based values (Peng et al., 2017) or by assigning identical E values to each land use type (Zhang et al., 2005), due to their lack of data on the components needed to calculate the gridded edaphic parameter E.

In this study, the Stefan equation with physically based parameters, as shown in Eq. (1), is adopted to simulate the MTSFG. Two main differences should exist between this equation and the simplified Stefan equation. First, the spatial distribution of the parameters in this study are determined using a physically based method with the combination of distributed temperature, precipitation and soil datasets based on remote sensing and ground observations, rather than simply assigning values according to land use classification or statistical interpolation of a lumped edaphic parameter E. The spatial distribution of the n-factor (Fig. 2a–b) is calculated using MODIS LST data, which is compared with

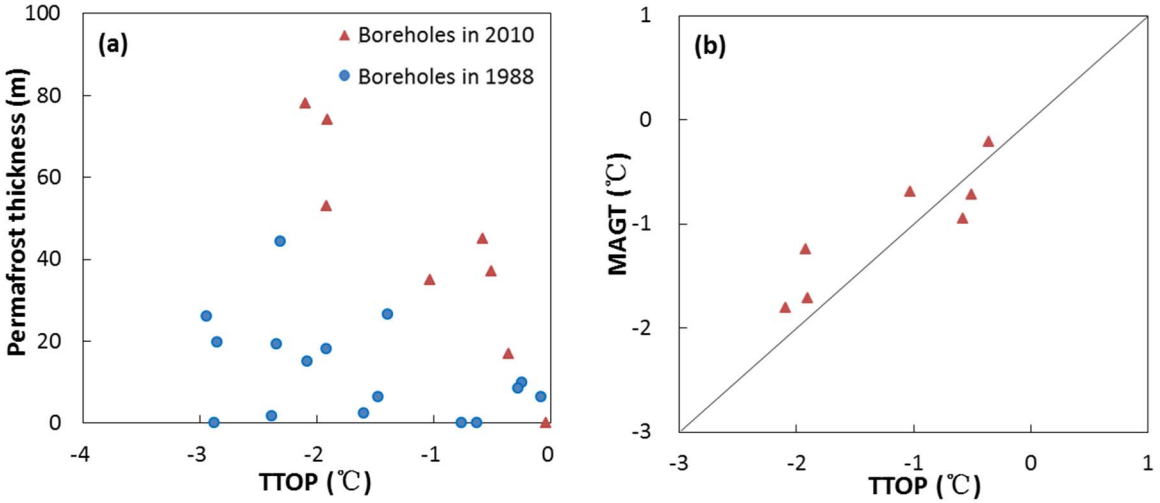

Fig. 6. Comparison of estimated TTOP values with (a) the borehole permafrost thickness and (b) the observed mean annual ground temperature (MAGT) at the zero annual amplitude depth.
Note: MAGT values at the zero annual amplitude depth are only available for the boreholes drilled in 2010. The boreholes drilled in 1988 are compared with the mean TTOP values during 1981–1990, and the boreholes drilled in 2010 are compared with the mean TTOP values during 2005–2014 derived from TTOP model.

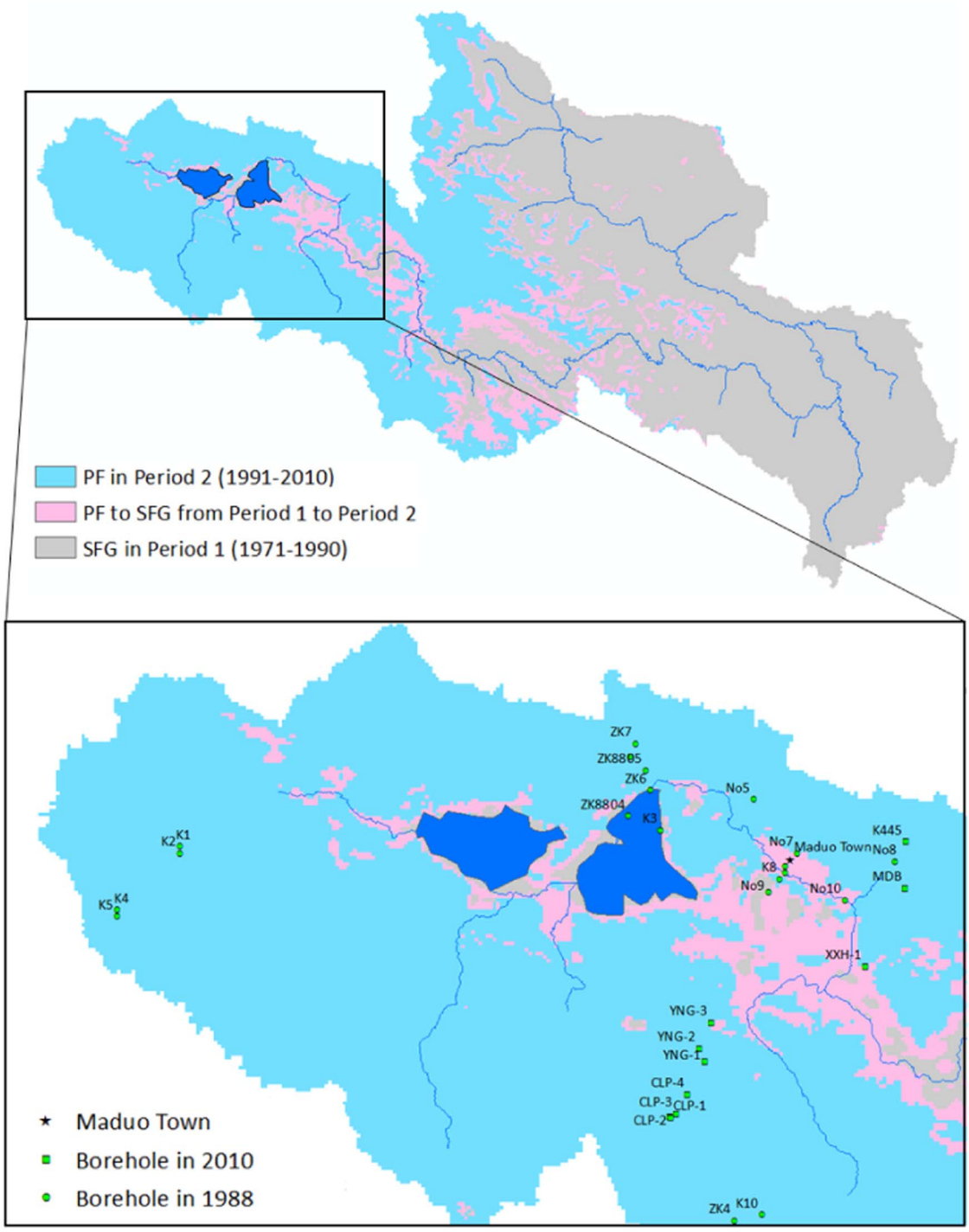

Fig. 7. Permafrost shrinkage and seasonally frozen ground sprawling from Period 1 (1971–1990) to Period 2 (1991–2010). Locations of the boreholes are marked.
Note: PF = permafrost and SFG = seasonally frozen ground. (For interpretation of the references to in this figure legend, the reader is referred to the web version of this article.)

the land use map obtained from the Cold and Arid Regions Science Data Center at Lanzhou (CARD) (http://westdc.westgis.ac.cn) (Fig. 2c). The spatial pattern of the n-factor calculated by MODIS LST data can reflect the differences among different land use types. For example, bare land tends to have larger n_f and n_t, as was also found in Canada (Smith et al., 2010), while wetland and irrigated cropland tend to have smaller n_t. Additionally, the spatial distribution of soil moisture is determined from the CSMDA dataset. The utilization of different datasets combining remote sensing and ground-based observations makes the estimation of the MTSFG spatial pattern more physically reasonable.

Second, the soil moisture in the Stefan equation is calculated by Eq. (2) using a variant of the antecedent precipitation index method in this study. Therefore, the edaphic parameter can fluctuate with time, and MTSFG fluctuations are derived from temperature as well as soil conditions, which should be closer to reality. In practice, however, the annual MTSFG time series considering soil property fluctuations showed little difference and little improvement, when compared with the time series considering soil moisture as a constant at most stations. This may result from the fact that interannual fluctuations in soil moisture are relatively small in magnitude, and the uncertainties in spatially distributed datasets, e.g., the CGDPA precipitation dataset, and the scale inconsistency between the grid and station scales might

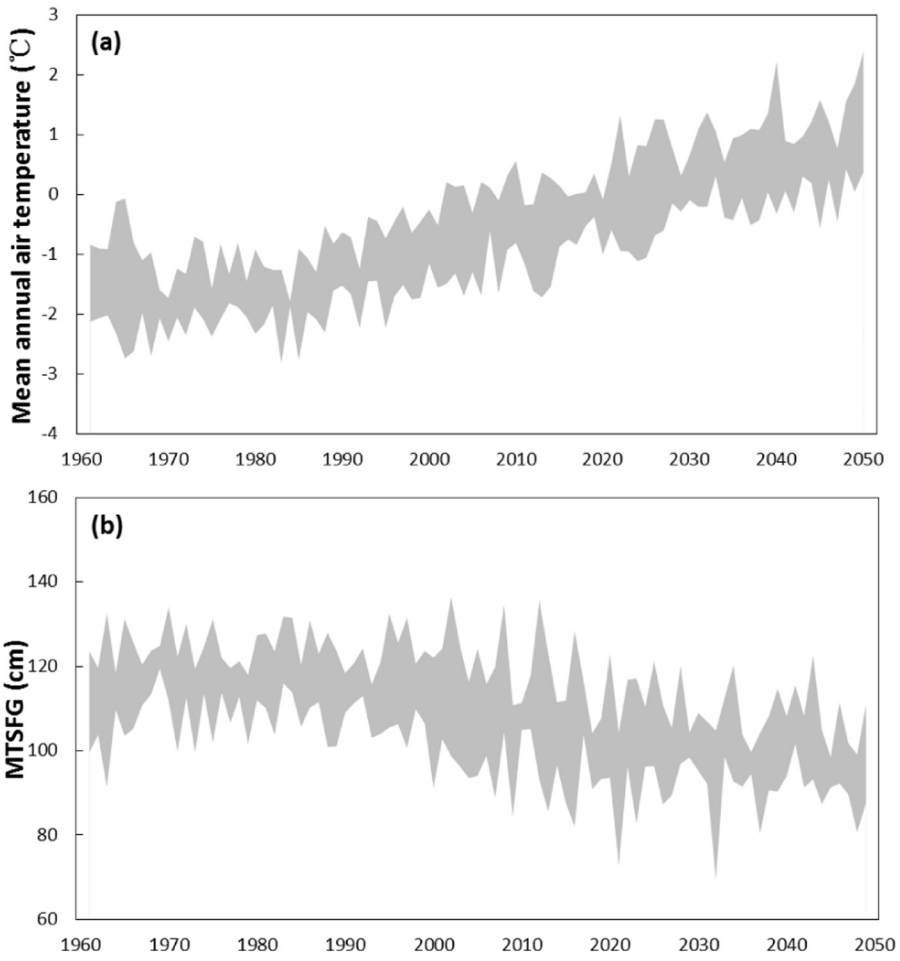

Fig. 8. Interannual variations in the (a) mean annual air temperature (MAAT) and (b) the areal mean MTSFG derived from 5 GCMs estimated by the Stefan equation.
Note: The shaded region represents the range estimated by the 5 GCMs (RCP 4.5).

Table 3
Comparison of the MTSFG estimated by the Stefan equation and mean annual air temperature (MAAT) derived from historical records and future climate under the RCP 4.5 scenario provided by 5 different GCMs.

Maximum thickness of seasonally frozen ground (MTSFG)					Mean annual air temperature (MAAT)				
	Historical period (1965–2014)		Future period (2015–2050)			Historical period (1965–2014)		Future period (2015–2050)	
	Multi-year average value (cm)	Long-term change rate (cm/10 a)	Multi-year average value (cm)	Long-term change rate (cm/10 a)		Multi-year average value (°C)	Long-term change rate (°C/10 a)	Multi-year average value (°C)	Long-term change rate (°C/10 a)
Historically observed data	124.64	−3.47*	\	\	Historically observed data	−2.13	0.42*	\	\
NorESM1-M	112.63	−3.01*	98.43	−2.34*	NorESM1-M	−1.27	0.32*	0.20	0.41*
MIROC-ESM-CHEM	117.97	−0.59	104.26	−2.38	MIROC-ESM-CHEM	−1.35	0.16*	0.63	0.40*
IPSL-CM5A-LR	112.51	−3.08*	98.42	−3.07*	IPSL-CM5A-LR	−1.22	0.37*	0.33	0.49*
HadGEM2-ES	111.26	−3.04*	99.62	−2.88	HadGEM2-ES	−1.20	0.38*	0.22	0.26*
GFDL-ESM2M	111.70	−2.24*	102.71	−1.69*	GFDL-ESM2M	−1.30	0.24*	−0.15	0.25*
Mean of 5 GCMs	113.21	−2.39*	100.69	−2.47*	Mean of 5 GCMs	−1.27	0.29*	0.25	0.36*

*Note: an asterisk following a value means the trend is significant at the 0.05 significance level.

counteract the improvements brought by the consideration of the interannual soil property fluctuations.

In this study, the estimated MTSFG values show a significant linear relationship with the observed MTSFG ($p < .05$) at all the 10 stations, and the overall *RMSE* is 21.25 cm (Table 1). The simulated results tend to overestimate the MTSFG at stations located in the Zoige wetland, including Zoige, Maqu and Hongyuan stations, but underestimate the MTSFG at high-elevation stations, including Guoluo and Dari stations. Although the Stefan equation yields good long-term trend estimates for most stations, differences between the observed and estimated MTSFG long-term trends still occur, and the largest underestimation occurs at Jiuzhi station (Table 1). This underestimation may be caused by the lack of a decreasing trend in the freezing season n-factor (n_f). The ground surface temperature is higher than the air temperature on the TP. At several stations, the ground surface temperature increases more rapidly than the air temperature, thus enlarging the gap between the two temperatures. As a result, n_f shows a decreasing trend for some stations in the UYRB, including Maqu, Jiuzhi and Henan stations, and the long-term MTSFG trends are underestimated for these stations. If the gap between the ground surface temperature and the air

Table 4
Permafrost area changes estimated by the TTOP model derived from historical records and future climate under the RCP 4.5 scenario provided by 5 different GCMs.

	Permafrost area (km^2)		
	1991–2010	2011–2030	2031–2050
Historical data	46,394		
NorESM1-M	44,499	38,187	27,199
MIROC-ESM-CHEM	44,252	31,236	18,633
IPSL-CM5A-LR	43,508	37,541	25,680
HadGEM2-ES	42,823	31,968	29,295
GFDL-ESM2M	46,093	40,223	33,867
mean of 5 GCMs	44,235	35,831	26,935

temperature continues to widen and the freezing season n-factor continues to decrease, then the future MTSFG in the UYRB will decrease at a more rapid rate relative to the predicted estimates in this study.

5.2. Frozen ground change compared with previous studies

This study estimates that the MTSFG in the UYRB decreased by 3.5 cm/10 a from 1965 to 2014 as the areal MAAT increased by 0.42 °C/10 a, and an abrupt acceleration has been observed since 1995, which is consistent with the results of other studies (Cuo et al., 2013). The MTSFG decreasing rate in the UYRB is lower than the rate of 7.4 cm/10 a during 1960–2014 in the upper Heihe River Basin, northeastern TP (Qin et al., 2016), while larger than the rate of 1.8 cm/10 a for seasonally frozen ground across China (Peng et al., 2017) during the period 1967–2012. The results indicate that the seasonally frozen ground on the margins of the TP is more sensitive to climate warming than the average of seasonally frozen ground regions in China.

This study uses the TTOP model to estimate the permafrost distribution and its changes. The permafrost area on the TP is estimated to have decreased by 30% from the 1970s to the 2000s by Cheng and Jin (2013) and by 16% from the 1980s to the 2000s by Xu et al. (2016), and the permafrost area in China is estimated to have decreased by 22% from 1980 to 2010 by Ran and Li (2016). These values are consistent with the 23% decrease in the UYRB estimated by the TTOP model in this study. The permafrost degradation in the UYRB was also observed at the point scale by in situ observations (Jin et al., 2009; Luo et al., 2012a), and these degradation results can be reflected by the TTOP model, as mentioned in Section 4.2.

Historical and future permafrost degradation trends have been estimated for other regions. The permafrost area in Canada is estimated to decrease by 24% by 2100 using a disequilibrium model (Y. Zhang et al., 2008) and by 43% using an equilibrium model (Kettles et al., 1997). The near-surface permafrost area of the TP is projected to decrease by approximately 39% by the mid-21st century and by approximately 81% by the end of the 21st century (Guo et al., 2012). In comparison, approximately 40% of the permafrost in 1991–2010 is projected to degrade into seasonally frozen ground in 2031–2050 in the UYRB estimated by the TTOP model in this study. It should be noted that the TTOP model is an equilibrium model and might underestimate permafrost extent in transient conditions due to the thermal inertia of permafrost (Riseborough, 2007; Ran and Li, 2016). On the other hand, the analytical models used in this study only consider the vertical heat transfer and neglect the lateral heat transfer, while the lateral heat transfer could accelerate permafrost degradation in the discontinuous permafrost region (Kurylyk et al., 2016) and in the alpine permafrost region (Noetzli et al., 2007). Models incorporating more physical processes are needed to analyze the transient effects and the impact of lateral heat transfer on permafrost degradation.

The changes in frozen ground profoundly impact the hydrology and ecology in UYRB by enhancing groundwater-surface water interaction, increasing the baseflow, and slowing down the winter recession (Niu et al., 2016; Qin et al., 2017; Wang et al., 2017). Many researchers hypothesize that the permafrost degradation could lower the groundwater table, reduce streamflow and influence the vegetation growth (Cheng and Wu, 2007; Jin et al., 2009; Yang et al., 2010). However, the future response of streamflow and vegetation to frozen ground degradation is still an open question. The GCM projections in this study can provide insights into the long-term trends of the MTSFG values and permafrost area in the UYRB, and can be taken into consideration when estimating long-term hydrological and vegetation changes and performing sustainable water resource management.

6. Conclusions

In this study, the Stefan equation and TTOP model with physically based parameters have been adopted to estimate the long-term trends and spatial variability in the frozen ground in the UYRB over the past 50 years and in the future. Comprehensive validation has been performed using long-term soil frozen depth and borehole observations. According to the results, the following conclusions have been reached:

1) The Stefan equation and TTOP model with physically based parameters combining both ground-based and remote sensing observations have been proved to be applicable in estimating the MTSFG and permafrost distribution in the UYRB.
2) As estimated by the Stefan equation, the MTSFG decreased at a rate of 3.47 cm/10 a from 1965 to 2014 as the areal mean MAAT increased at a rate of 0.42 °C/10 a. The most rapid decrease in MTSFG values occurred in the transitional zone between permafrost and seasonally frozen ground around Xinghai station. Approximately 23% of the permafrost area degraded to seasonally frozen ground during the past 50 years according to the TTOP model.
3) The areal mean MTSFG is projected to decrease at a rate of 1.69 to 3.07 cm/10 a during 2015–2050 using the climate data simulated by 5 GCMs under RCP 4.5. Approximately 40% of the permafrost in 1991–2010 is projected to degrade into seasonally frozen ground in 2031–2050 according to the TTOP model.

This study provides a framework for estimating the long-term changes in frozen ground using multi-source observations and minimal parameterizations, and it can be applied to other locations on the TP. The changes in frozen ground could result in complex feedback mechanisms with hydrological processes and vegetation growth. Therefore, developing a better understanding of frozen ground changes provides a scientific basis for future studies on interactions between frozen ground changes and ecohydrological processes under a changing climate.

Acknowledgements

This research was supported by the National Natural Science Foundation of China (NSFC Project No. 41630856, 91225302 and 91425303). The authors would like to thank CMA for providing the observation data for soil temperatures and soil frozen depths on the TP. The authors thank the editor and the anonymous reviewers for their constructive and detailed comments.

References

Bense, V.F., Kooi, H., Ferguson, G., Read, T., 2012. Permafrost degradation as a control on hydrogeological regime shifts in a warming climate. J. Geophys. Res. Earth Surf. 117 (F3).
Chen, S.Y., et al., 2012. Response characteristics of vegetation and soil environment to permafrost degradation in the upstream regions of the Shule River Basin. Environ. Res. Lett. 7 (4).
Chen, Z., Lei, H., Yang, H., Yang, D., Cao, Y., 2017. Historical and future trends in wetting and drying in 291 catchments across China. Hydrol. Earth Syst. Sci. 21 (4), 2233.
Cheng, G.D., Jin, H.J., 2013. Permafrost and groundwater on the Qinghai-Tibet Plateau and in northeast China. Hydrogeol. J. 21 (1), 5–23.

Cheng, G.D., Wu, T.H., 2007. Responses of permafrost to climate change and their environmental significance, Qinghai-Tibet Plateau. J. Geophys. Res. Earth Surf. 112 (F2).
CMA, 2007a. Specifications for Surface Meteorological Observation. Part13: Measurement of Soil Temperature. China Meteorological Press, Beijing, China (In Chinese).
CMA, 2007b. Specifications for Surface Meteorological Observation. Part14: Measurement of Frozen Soil. China Meteorological Press, Beijing, China (In Chinese).
Cuo, L., Zhang, Y., Gao, Y., Hao, Z., Cairang, L., 2013. The impacts of climate change and land cover/use transition on the hydrology in the upper Yellow River Basin, China. J. Hydrol. 502, 37–52.
Cuo, L., et al., 2015. Frozen soil degradation and its effects on surface hydrology in the northern Tibetan Plateau. J. Geophys. Res.-Atmos. 120 (16), 8276–8298.
Fang, Y.P., Qin, D.H., Ding, Y.J., 2011. Frozen soil change and adaptation of animal husbandry: a case of the source regions of Yangtze and Yellow Rivers. Environ. Sci. Pol. 14 (5), 555–568.
FAO, I., ISRIC, I., 2009. JRC (2009) Harmonized World Soil Database (Version 1.1). FAO, Rome, Italy and IIASA, Laxenburg, Austria [www document]. URL. http://www.fao.org/nr/land/soils/harmonized-world-soildatabase/en.
Farouki, O.T., 1981. The thermal-properties of soils in cold regions. Cold Reg. Sci. Technol. 5 (1), 67–75.
Frauenfeld, O.W., 2004. Interdecadal changes in seasonal freeze and thaw depths in Russia. J. Geophys. Res.-Atmos. 109 (D5).
Frauenfeld, O.W., Zhang, T.J., 2011. An observational 71-year history of seasonally frozen ground changes in the Eurasian high latitudes. Environ. Res. Lett. 6 (4), 044024.
Frauenfeld, O.W., Zhang, T.J., McCreight, J.L., 2007. Northern hemisphere freezing/thawing index variations over the twentieth century. Int. J. Climatol. 27 (1), 47–63.
Guo, D., Wang, H., 2013. Simulation of permafrost and seasonally frozen ground conditions on the Tibetan Plateau, 1981–2010. J. Geophys. Res. Atmos. 118 (11), 5216–5230.
Guo, D., Wang, H., Li, D., 2012. A projection of permafrost degradation on the Tibetan Plateau during the 21st century. J. Geophys. Res.-Atmos. 117 (D5).
Hayashi, M., 2013. The cold vadose zone: hydrological and ecological significance of frozen-soil processes. Vadose Zone J. 12 (4).
Hu, Y.R., Maskey, S., Uhlenbrook, S., Zhao, H.L., 2011. Streamflow trends and climate linkages in the source region of the Yellow River, China. Hydrol. Process. 25 (22), 3399–3411.
Immerzeel, W.W., van Beek, L.P.H., Bierkens, M.F.P., 2010. Climate change will affect the Asian water towers. Science 328 (5984), 1382–1385.
Jarvis, A., Reuter, H.I., Nelson, A., Guevara, E., 2008. Hole-filled Seamless SRTM Data V4. International Centre for Tropical Agriculture (CIAT).
Jin, H.J., et al., 2009. Changes in frozen ground in the source area of the Yellow River on the Qinghai-Tibet Plateau, China, and their eco-environmental impacts. Environ. Res. Lett. 4 (4).
Jin, R., Zhang, T., Li, X., Yang, X., Ran, Y., 2015. Mapping surface soil freeze-thaw cycles in China based on SMMR and SSM/I brightness temperatures from 1978 to 2008. Arct. Antarct. Alp. Res. 47 (2), 213–229.
Kettles, I., Tarnocai, C., Bauke, S., 1997. Predicted permafrost distribution in Canada under a climate warming scenario. In: Current Research, Geological Survey of Canada. 1997-E. pp. 109–115.
Klene, A.E., Nelson, F.E., Shiklomanov, N.I., Hinkel, K.M., 2001. The n-factor in natural landscapes: variability of air and soil-surface temperatures, Kuparuk River basin, Alaska, USA. Arct. Antarct. Alp. Res. 33 (2), 140–148.
Krause, P., Boyle, D., Bäse, F., 2005. Comparison of different efficiency criteria for hydrological model assessment. Adv. Geosci. 5, 89–97.
Kurylyk, B.L., Hayashi, M., 2016. Improved Stefan equation correction factors to accommodate sensible heat storage during soil freezing or thawing. Permafr. Periglac. Process. 27 (2), 189–203.
Kurylyk, B.L., Hayashi, M., Quinton, W.L., McKenzie, J.M., Voss, C.I., 2016. Influence of vertical and lateral heat transfer on permafrost thaw, peatland landscape transition, and groundwater flow. Water Resour. Res. 52 (2), 1286–1305.
Lee, K.T., Huang, J.-K., 2013. Runoff simulation considering time-varying partial contributing area based on current precipitation index. J. Hydrol. 486, 443–454.
Li, X., et al., 2008. Cryospheric change in China. Glob. Planet. Chang. 62 (3–4), 210–218.
Li, Q., Sun, S.F., Xue, Y.K., 2010. Analyses and development of a hierarchy of frozen soil models for cold region study. J. Geophys. Res.-Atmos. 115 (D3).
Liu, G.S., Wang, G.X., 2012. Insight into runoff decline due to climate change in China's water tower. Water Sci. Technol. Water Supply 12 (3), 352–361.
Liu, J.S., Xie, J., Gong, T.L., Wang, H., Xie, Y.H., 2011. Impacts of winter warming and permafrost degradation on water variability, upper Lhasa River, Tibet. Quat. Int. 244 (2), 178–184.
Luo, D.L., et al., 2012a. Degradation of permafrost and cold-environments on the interior and eastern Qinghai Plateau. J. Glaciol. Geocryol. 34 (3), 538–546 (in Chinese).
Luo, D.L., et al., 2012b. New progress on permafrost temperature and thickness in the source area of the Huanghe River. Sci. Geogr. Sin. 32 (7), 898–904 (in Chinese).
Luo, D.L., et al., 2016. Recent changes in the active layer thickness across the northern hemisphere. Environ. Earth Sci. 75 (7), 1–15.
Nan, Z.T., Li, S.X., Cheng, G.D., 2005. Prediction of permafrost distribution on the Qinghai-Tibet Plateau in the next 50 and 100 years. Sci. China Ser. D Earth Sci. 48 (6), 797–804.
Niu, L., et al., 2016. Response of hydrological processes to permafrost degradation from 1980 to 2009 in the Upper Yellow River Basin, China. Hydrol. Res. 47 (5), 1014–1024.
Noetzli, J., Gruber, S., Kohl, T., Salzmann, N., Haeberli, W., 2007. Three-dimensional distribution and evolution of permafrost temperatures in idealized high-mountain topography. J. Geophys. Res. Earth Surf. 112 (F2).
Pan, F., Peters-Lidard, C.D., Sale, M.J., 2003. An analytical method for predicting surface soil moisture from rainfall observations. Water Resour. Res. 39 (11).
Pang, Q., Zhao, L., Li, S., Ding, Y., 2011. Active layer thickness variations on the Qinghai–Tibet Plateau under the scenarios of climate change. Environ. Earth Sci. 66 (3), 849–857.
Park, H., et al., 2013. The influence of climate and hydrological variables on opposite anomaly in active-layer thickness between Eurasian and North American watersheds. Cryosphere 7 (2), 631–645.
Peng, X., et al., 2016. Response of changes in seasonal soil freeze/thaw state to climate change from 1950 to 2010 across China. J. Geophys. Res. Earth Surf. 121 (11), 1984–2000.
Peng, X., et al., 2017. Response of seasonal soil freeze depth to climate change across China. Cryosphere 11 (3), 1059.
Piani, C., et al., 2010. Statistical bias correction of global simulated daily precipitation and temperature for the application of hydrological models. J. Hydrol. 395 (3–4), 199–215.
Qin, Y., et al., 2016. Long-term change in the depth of seasonally frozen ground and its ecohydrological impacts in the Qilian Mountains, northeastern Tibetan Plateau. J. Hydrol. 542, 204–221.
Qin, Y., et al., 2017. Impacts of climate warming on the frozen ground and eco-hydrology in the Yellow River source region, China. Sci. Total Environ. 605–606, 830–841.
Qiu, J., 2008. China: the third pole. Nature 454 (7203), 393–396.
Ran, Y., Li, X., 2016. Evaluation of the permafrost stability degradation from 1980 to 2010 in China. Sci. Cold Arid Reg. 8 (5), 359–366.
Riseborough, D., 2007. The effect of transient conditions on an equilibrium permafrost-climate model. Permafr. Periglac. Process. 18 (1), 21–32.
Riseborough, D., Shiklomanov, N., Etzelmuller, B., Gruber, S., Marchenko, S., 2008. Recent advances in permafrost modelling. Permafr. Periglac. Process. 19 (2), 137–156.
Shen, Y., Xiong, A.Y., 2016. Validation and comparison of a new gauge-based precipitation analysis over mainland China. Int. J. Climatol. 36 (1), 252–265.
Smith, S., et al., 2010. Thermal state of permafrost in North America: a contribution to the international polar year. Permafr. Periglac. Process. 21 (2), 117–135.
Teng, W., Wang, J., Doraiswamy, P., 1993. Relationship between satellite microwave radiometric data, antecedent precipitation index, and regional soil moisture. Int. J. Remote Sens. 14 (13), 2483–2500.
Vaughan, D.G., et al., 2013. Observations: cryosphere. Clim. Chang. 317–382.
Walvoord, M.A., Kurylyk, B.L., 2016. Hydrologic impacts of thawing permafrost—a review. Vadose Zone J. 15 (6).
Wan, Z., 2007. Collection-5 MODIS Land Surface Temperature Products users' Guide. ICESS, University of California, Santa Barbara.
Wang, K., Zhang, T., Zhong, X., 2015. Changes in the timing and duration of the near-surface soil freeze/thaw status from 1956 to 2006 across China. Cryosphere 9 (3), 1321–1331.
Wang, Q.F., Zhang, T.J., Peng, X.Q., Cao, B., Wu, Q.B., 2015. Changes of soil thermal regimes in the Heihe River Basin over Western China. Arct. Antarct. Alp. Res. 47 (2), 231–241.
Wang, X., Chen, R., Yang, Y., 2017. Effects of permafrost degradation on the hydrological regime in the source regions of the Yangtze and Yellow Rivers, China. Water 9 (11), 897.
Warszawski, L., et al., 2014. The Inter-Sectoral Impact Model Intercomparison Project (ISI-MIP): project framework. Proc. Natl. Acad. Sci. U. S. A. 111 (9), 3228–3232.
Woo, M.K., 2012. Permafrost Hydrology. Springer Science & Business Media.
Wu, Q.B., Zhang, T.J., 2010. Changes in active layer thickness over the Qinghai-Tibetan Plateau from 1995 to 2007. J. Geophys. Res.-Atmos. 115 (D9).
Wu, Q., Zhang, T., Liu, Y., 2010. Permafrost temperatures and thickness on the Qinghai-Tibet Plateau. Glob. Planet. Chang. 72 (1), 32–38.
Wu, Q.B., Hou, Y.D., Yun, H.B., Liu, Y.Z., 2015. Changes in active-layer thickness and near-surface permafrost between 2002 and 2012 in alpine ecosystems, Qinghai-Xizang (Tibet) Plateau, China. Glob. Planet. Chang. 124, 149–155.
Xie, C., Zhao, L., Wu, T., Dong, X., 2012. Changes in the thermal and hydraulic regime within the active layer in the Qinghai-Tibet Plateau. J. Mt. Sci.-Engl. 9 (4), 483–491.
Xu, J.X., 2015. Complex response of runoff-precipitation ratio to the rising air temperature: the source area of the Yellow River, China. Reg. Environ. Chang. 15 (1), 35–43.
Xu, X., Zhang, Z., Wu, Q., 2016. Simulation of permafrost changes on the Qinghai–Tibet Plateau, China, over the past three decades. Int. J. Digital Earth 1–17.
Yang, D., et al., 2004. Analysis of water resources variability in the Yellow River of China during the last half century using historical data. Water Resour. Res. 40 (6).
Yang, M.X., Nelson, F.E., Shiklomanov, N.I., Guo, D.L., Wan, G.N., 2010. Permafrost degradation and its environmental effects on the Tibetan Plateau: a review of recent research. Earth-Sci. Rev. 103 (1–2), 31–44.
Yang, K., et al., 2016. Land surface model calibration through microwave data assimilation for improving soil moisture simulations. J. Hydrol. 533, 266–276.
Yin, G., Niu, F., Lin, Z., Luo, J., Liu, M., 2016. Performance comparison of permafrost models in Wudaoliang Basin, Qinghai-Tibet Plateau, China. J. Mt. Sci.-Engl. 13 (7), 1162–1173.
Zhang, T., Barry, R.G., Knowles, K., Ling, F., Armstrong, R.L., 2003. Distribution of seasonally and perennially frozen ground in the Northern Hemisphere. Permafrost 1 and 2, 1289–1294.
Zhang, T.J., et al., 2005. Spatial and temporal variability in active layer thickness over the Russian Arctic drainage basin. J. Geophys. Res.-Atmos. 110 (D16).
Zhang, Y., Chen, W., Riseborough, D.W., 2008. Disequilibrium response of permafrost thaw to climate warming in Canada over 1850–2100. Geophys. Res. Lett. 35 (2).
Zhang, Y.S., Carey, S.K., Quinton, W.L., 2008. Evaluation of the algorithms and parameterizations for ground thawing and freezing simulation in permafrost regions. J.

Geophys. Res.-Atmos. 113 (D17).
Zhang, W.J., Yi, Y.H., Song, K.C., Kimball, J.S., Lu, Q.F., 2016. Hydrological response of alpine wetlands to climate warming in the eastern Tibetan Plateau. Remote Sens. (Basel) 8 (4).
Zhang, Y., et al., 2016. Influences of frozen ground and climate change on hydrological processes in an Alpine watershed: a case study in the upstream area of the Hei'he River, Northwest China. Permafr. Periglac. Process. 28 (2), 420–432.
Zhao, S.P., Nan, Z.T., Huang, Y.B., Zhao, L., 2017. The application and evaluation of simple permafrost distribution models on the Qinghai–Tibet Plateau. Permafr. Periglac. Process. 28 (2), 391–404.
Zou, D., et al., 2014. Modeling ground surface temperature by means of remote sensing data in high-altitude areas: test in the central Tibetan Plateau with application of moderate-resolution imaging spectroradiometer Terra/Aqua land surface temperature and ground-based infrared radiometer. J. Appl. Remote. Sens. 8 (1), 083516.
Zou, D., et al., 2017. A new map of permafrost distribution on the Tibetan Plateau. Cryosphere 11 (6), 2527.